Simulation of Shock-Induced Combustion Past Blunt Projectiles Using Shock-Fitting Technique

J. K. Ahuja*
Old Dominion University, Norfolk, Virginia 23529
A. Kumar†
NASA Langley Research Center, Hampton, Virginia 23681
D. J. Singh‡
Analytical Services and Materials, Inc., Hampton, Virginia 23666
and
S. N. Tiwari§
Old Dominion University, Norfolk, Virginia 23529

Two-dimensional axisymmetric, reacting viscous flow over blunt projectiles is computed to study shock-induced combustion at Mach 5.11 and 6.46 in hydrogen–air mixture. A finite difference, shock-fitting method is used to solve the complete set of Navier–Stokes and species conservation equations. In this approach, the bow shock represents a boundary of the computational domain and is treated as a discontinuity across which Rankine–Hugoniot conditions are applied. All interior details of the flow such as compression waves, reaction front, and the wall boundary layer are captured automatically in the solution. Since the shock-fitting approach reduces the amount of artificial dissipation, all intricate details of the flow are captured much more clearly than has been possible with the shock-capturing approach. This has allowed an improved understanding of the physics of shock-induced combustion over blunt projectiles and the numerical results can now be explained more readily with a one-dimensional wave-interaction model.

Nomenclature

F, G = flux vectors
H = source vectors
h_i^R = base enthalpy of ith species
i_r = unit vector along radius r, i.e., normal to the body
i_θ = unit vector tangential to the body
J = Jacobian
k = thermal conductivity
M_i = molecular weight of ith species
n = unit vector normal to the shock
p = pressure
R_i = gas constant of ith species
r_n = nose radius
r_{s_i} = radial shock velocity
S = unit vector tangential to the shock
T = temperature
t = time
U = dependent variable vector
U_S = local shock velocity
u = x component of the velocity
u_∞ = velocity tangential to the body
v = y component of the velocity
v_∞ = velocity normal to the body
x = streamwise coordinate in the physical domain
y = normal coordinate in the physical domain
η = normal coordinate in the computational domain

θ = angle the radius makes with the x axis, i.e., body angle
ξ = streamwise coordinate in the computational domain
ρ = density

Introduction

ONE of the propulsion concepts for hypersonic vehicles is the proposed oblique detonation wave engine.[1-3] In this concept, an oblique shock wave in the combustor is employed to increase the temperature of premixed fuel and air to a point where chemical reaction can start. It can be utilized to provide a smaller, lightweight engine or to provide a higher payload capability for a given vehicle weight.

In the past, many researchers[4-7] have conducted ballistic range experiments to study supersonic combustion/detonation. In these experiments, projectiles were fired in different fuel–air mixtures, and detonation structures around the projectiles were recorded. Every gas mixture has a detonation wave velocity known as Chapman–Jouget (C–J) velocity, which is characteristic of the mixture. If the velocity of the projectile is above the C–J velocity of the reactive mixture, the freestream velocity is referred to as overdriven. On the other hand, if the projectile velocity is lower than the C–J velocity, the freestream velocity is referred to as underdriven. There is a progression of higher frequency and lower amplitude oscillations as the Mach number is increased with a steady flow observed at some point above the C–J velocity. If the projectile is flying above the C–J velocity of the gas mixture, the detonation or reaction front structure shows a coupled shock-deflagration system near the stagnation line of the body. These two fronts separate from each other as one moves away from the stagnation line. The separation between the two fronts occurs as soon as the velocity component normal to the bow shock is equal to the detonation velocity. The separation between the bow shock and the reaction front is called the induction zone.

*Graduate Research Assistant, Department of Mechanical Engineering.
†Chief, Gas Dynamics Division. Fellow AIAA.
‡Senior Research Scientist, Analytical Section.
§Eminent Professor, Department of Mechanical Engineering. Associate Fellow AIAA.

In 1972 Lehr[4] conducted a detailed experimental study for a wide range of projectile shapes and combustible mixtures. The projectile shapes tested included not only spheres, but cones, bicones, and flat-nose projectiles. The mixtures included hydrogen–air, hydrogen–oxygen, methane–air, and methane–oxygen. Ballistic range shadowgraph pictures for Mach 5.11 and 6.46 from Lehr's experiments are shown in Figs. 1 and 2, respectively. In both cases, a freestream temperature of 292 K and a pressure of 42,663.2 N/m^2 (320 mm of Hg) is used along with a stoichiometric mixture of hydrogen–air. The projectile diameter was 15 mm. At these conditions the C–J Mach number of the mixture is 4.85. The shadowgraph in Fig. 1 shows two discontinuities separated from each other. The outer front is the bow shock and the inner front is the reaction front produced by ignition of the heated H_2–air mixture. The separation between the two is minimum near the stagnation point and increases as the shock curves around the body, due to an increase in induction distance (decrease in postshock temperature) away from the stagnation zone. A close examination of the shadowgraphs reveals that as the flow crosses the bow shock, the color changes from light to dark, indicating an increase in density. But, as the flow crosses the reaction front, the color changes from dark to light, indicating a decrease in density across the reaction front. This is due to a large release of energy across the reaction front, causing an increase in the temperature; since the pressure remains relatively constant, the density must decrease. Another interesting feature is the presence of corrugation in the reaction front. These corrugations are caused by the pulsation of the reaction front. The frequency of this pulsation was determined to be 1.96 MHz.[5] Figure 2 is for the Mach 6.46 case, and it is seen that the reaction front is coupled with the shock near the stagnation line and up to about a 60–65-deg body angle from the stagnation line. This is because of a very high postshock temperature at Mach 6.46 that causes the induction zone to become so narrow that it appears that the two fronts are merged with each other. Decoupling begins further downstream from the stagnation line when the postshock temperature starts decreasing and, therefore, the induction distance increases. Further, both the bow shock and the reaction fronts are smooth without any visible instabilities. Thus, for an overdriven case of Mach 6,46, the instabilities have disappeared. References 4 and 5 show other underdriven cases where it has been shown that the instabilities in the reaction front become more pronounced as we reduce the projectile velocity lower than the C–J velocity of the mixture. In all of these cases the projectile diameter was fixed as 15 mm. Several researchers[8–16] have attempted to numerically simulate Lehr's ballistic range experiments.[4] These are discussed in detail in Refs. 15–17.

The key parameters for the triggering of instabilities have been identified by various parametric studies.[16–18] Matsuo and Fujiwara[16] and Ahuja and Tiwari[17] demonstrated that an underdriven case, which shows instabilities in the reaction front, can be made stable by having an appropriately small-size projectile, and an overdriven case can be made unstable by having a large-size projectile. Kumar and Singh[18] concluded that the key parameters for triggering these instabilities were projectile velocity, activation temperature, projectile nose radius, reaction rate constant, and heat release.

Tivanov and Rom[19] conducted an analytical study based on an energy equation and a chemical rate equation for the flow of a detonable gas mixture over a blunt body. They evaluated the conditions for the stability of the detonation process and the appearance of the oscillations. The frequency of oscillations matched very well with the experimental data.

Matsuo et al.[20] conducted a parametric study for regular and large disturbance regimes of shock-induced combustion using a two-step chemistry model. With a series of simulations the large disturbance regime was explained with their new proposed model. Their results revealed that the intensity of heat release was a key parameter in determining the regime of the
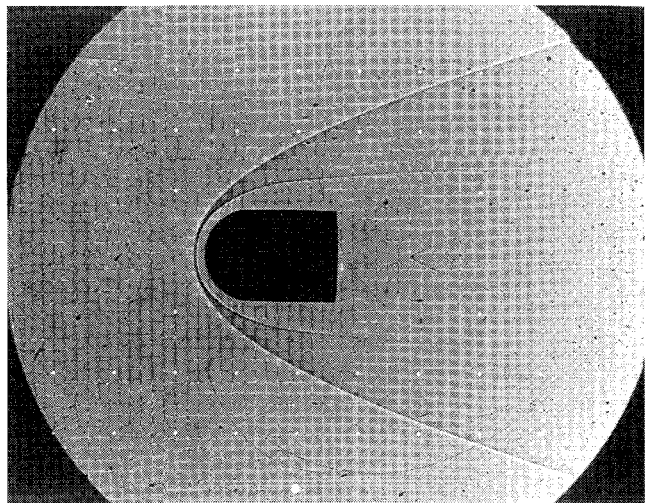

Fig. 1 Shadowgraph of a spherical nose projectile moving at Mach 5.11 into a premixed stoichiometric hydrogen–air mixture.
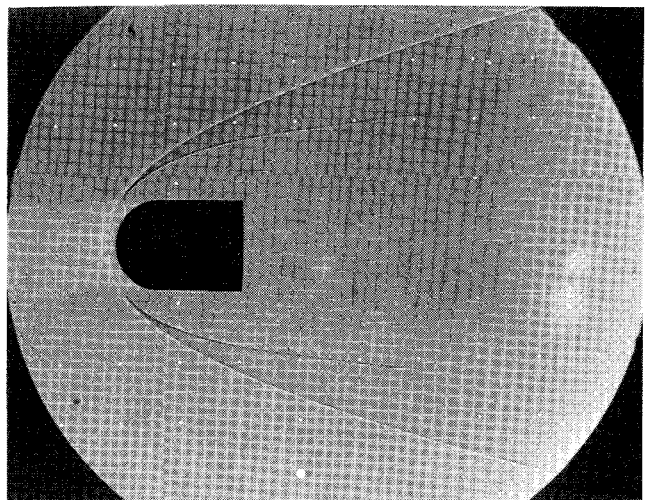

Fig. 2 Shadowgraph of a spherical nose projectile moving at Mach 6.46 into a premixed stoichiometric hydrogen–air mixture.

unsteady flow. Flow features of the unsteady combustion with low-frequency and high-amplitude oscillation, known as large-disturbance regimes, are reproduced when the concentration of the heat release is very high. For moderately high heat release, a high-frequency, low-amplitude periodic unsteadiness that belongs to regular regimes was observed. Ruegg and Dorsey[21] observed the same phenomena experimentally.

In problems like shock-induced combustions where physical instabilities are present, the shock-capturing methods will smear some of the instabilities. Thus, shock-capturing methods, when used in complicated problems of practical interest, would not reproduce many of the intricate flow features. On the other hand, in the shock-fitting approach, one knows the precise location of the discontinuity that acts as one of the boundaries of the flowfield, across which Rankine–Hugoniot conditions are applied. This approach avoids taking differences across the shock and the smearing of the shock that occur in the shock-capturing method. There are some obvious advantages of shock fitting over shock capturing. Shock fitting requires far less grid points compared to shock capturing. In shock capturing the bow shock becomes a smeared shock surface and requires more grid points for the extension of the grid in the freestream region. This adds to the savings in computational time in shock fitting as compared to shock capturing. Since very small dissipation is needed in shock fitting, the

intricate details of the flow can be reproduced, as the dissipation does not smear the important flow features.

The present study investigates, in detail, the shock-induced combustion phenomena for a premixed stoichiometric H_2–air mixture flow at hypersonic speeds (Mach 5.11 and 6.46), using the shock-fitting technique past a 15-mm spherical projectile. These are the first such simulations done with shock fitting for the ballistic range experiments. The analysis is carried out using the axisymmetric version of the SPARK2D code[22] with shock-fitting capability, which incorporates a seven-species, seven-reactions combustion model for hydrogen–air mixtures.
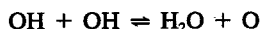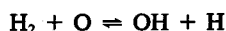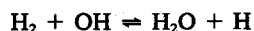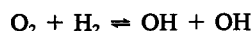
Basic Governing Equations

The physical model for analyzing the flowfield is described by the Navier–Stokes and species continuity equations. For two-dimensional axisymmetric flows, these equations are expressed in physical coordinates as

$$\frac{\partial U}{\partial t} + \frac{\partial F}{\partial x} + \frac{\partial G}{\partial y} = H \quad (1)$$

The vectors U, F, G, and H are defined in Ref. 22, where other relevant equations are also available.

The hydrogen–air combustion mechanism used in this work is based on the Jachimowski hydrogen–air model,[23] which uses seven species and seven reactions. The species are N_2, O_2, H_2, OH, H_2O, O, and H. Each of the seven reactions can proceed in the forward and backward directions. The reactions are

$$O_2 + H_2 \rightleftharpoons OH + OH$$

$$O_2 + H \rightleftharpoons OH + O$$

$$H_2 + OH \rightleftharpoons H_2O + H$$

$$H_2 + O \rightleftharpoons OH + H$$

$$OH + OH \rightleftharpoons H_2O + O$$

$$OH + H + M \rightleftharpoons H_2O + M$$

$$H + H + M \rightleftharpoons H_2 + M$$

The stoichiometric chemical reaction for a hydrogen–air system can be written as

$$2H_2 + O_2 + 3.76N_2 \rightarrow 2H_2O + 3.76N_2$$
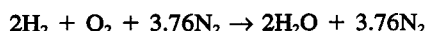
For a blunt body moving through a reactive mixture at hypersonic speeds, the temperature of the fuel–air mixture after the bow shock is sufficiently high to initiate the reaction. Once the ignition starts, chemical energy is released and the reaction front is formed. In the induction zone, the temperature and pressure remain relatively constant at the postshock conditions, while the concentrations of radicals build up very rapidly.

Method of Solution

The governing equations of motion are transformed from physical space (x, y) to the computational domain (ξ, η) by the following relations:

$$\tau = t, \qquad \xi = \xi(t, x, y), \qquad \eta = \eta(t, x, y)$$

The final form of the governing equation in the computational domain with time-dependent terms is given by

$$\frac{\partial \hat{U}}{\partial \tau} + \frac{\partial \hat{F}}{\partial \xi} + \frac{\partial \hat{G}}{\partial \eta} = \hat{H} \quad (2)$$

In expanded form, the preceding equation can be written as

$$\left(\underbrace{\hat{U}}_{J^{-1}U}\right)_\tau + \left(\underbrace{\hat{F}}_{[\{-x_\tau y_\eta + x_\eta y_\tau\}U + y_\eta F - x_\eta G]}\right)_\xi$$

$$+ \left(\underbrace{\hat{G}}_{[\{x_\tau y_\xi - x_\xi y_\tau\}U - y_\xi F + x_\xi G]}\right)_\eta$$

$$= \underbrace{J^{-1}H + \overbrace{[U\{-x_\tau y_\eta + x_\eta y_\tau\}_\xi + U\{x_\tau y_\xi - x_\xi y_\tau\}_\eta]}^{\text{GCL TERMS}}}_{\hat{H}}$$

$$+ \overbrace{[F(y_\eta)_\xi - F(y_\xi)_\eta - G(x_\eta)_\xi + G(x_\xi)_\eta]}^{\text{GCL TERMS}} \quad (3)$$

In Eq. (3) terms that add to zero analytically, but numerically are not zero, are referred to as GCL (geometric conservation law correction) terms.

Boundary Conditions

The flow conditions behind the bow shock are determined by Rankine–Hugoniot relations. The shock boundary is allowed to move until it reaches a steady-state position. Figure 3 shows the coordinate transformation used in the shock-fitting procedure. The vector V_1 represents the vector component of the fluid velocity normal to (and measured with respect to) the moving shock. Therefore, one may express

$$V_1 = \{[V_\infty - U_S] \cdot n\}n = \{(v_\infty i_r \cdot n + u_\infty i_\theta \cdot n - U_S \cdot n) \cdot n\} \quad (4)$$

Consequently, the magnitude of the shock velocity in the direction normal to the body (i.e., along the radius) is given by

$$r_{S_t} = V_1[1 + (r_{S_\theta}/r_S)^2]^{1/2} + v_\infty - u_\infty(r_{S_\theta}/r_S) \quad (5)$$

The derivative $r^n_{S_\theta}$, which appears in Eq. (5), is evaluated by using the second-order central difference formula as

$$r^n_{S_{\theta(j)}} = \frac{[r^n_{S_{\theta(j+1)}} - r^n_{S_{\theta(j-1)}}]}{2\Delta\theta} \quad (2 \le j \le nny - 1) \quad (6)$$

At the beginning of the predictor step, the shock wave radial distance is computed from the Euler predictor equation

$$r_S^{\overline{n+1}} = r_S^n + \Delta t r_{S_t}^n \quad (7)$$

Therefore,

$$V_1 = V_1 \cdot n = v_1 i_r + u_1 i_\theta \quad (8)$$

where v_1 = component of fluid velocity V_1 normal to the body (i.e., along i_r direction) and u_1 = component of the fluid velocity V_1 tangential to the body (i.e., along i_θ direction). Therefore,

$$u_1 = -\frac{(r_{S_\theta}/r_S)}{[1 + (r_{S_\theta}/r_S)^2]} [r_{S_t} - v_\infty + u_\infty(r_{S_\theta}/r_S)] \quad (9)$$

$$v_1 = [r_{S_t} - v_\infty + u_\infty(r_{S_\theta}/r_S)] \frac{1}{\sqrt{1 + (r_{S_\theta}/r_S)^2}} \quad (10)$$
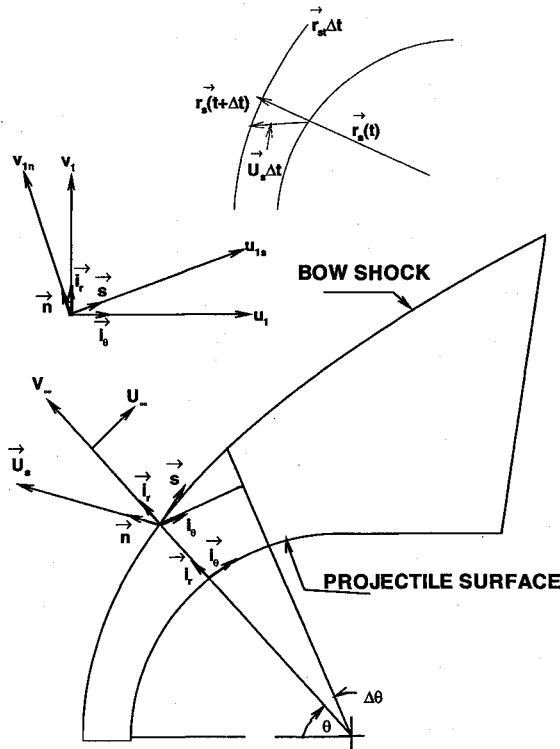
Fig. 3 Notation and coordinate system used for shock-fitting method.

Let u_{1S} = velocity component tangent to the shock (i.e., in s direction) and v_{1n} = velocity component normal to the shock (i.e., in n direction). Then, by applying shock jump conditions, we have

$$\rho_1 v_{1n} = \rho_2 v_{2n} \tag{11}$$

Since tangential velocity is preserved, then

$$u_{2S} = u_{1S} \tag{12}$$

Let V_2 = resultant velocity after the shock with respect to shock coordinates. Therefore, $V_2 = v_{2n}n + u_{2S}S$. The component of V_2 along i_θ (i.e., tangent to the body) is given by

$$u_2 = V_2 \cdot i_\theta \tag{13}$$

Similarly, the component of V_2 along i_r (i.e., normal to the body) is given by

$$v_2 = V_2 \cdot i_r \tag{14}$$

Therefore,

$$u_2 = u_\infty - \left(1 - \frac{\rho_1}{\rho_2}\right) \times \frac{[r_{S_t} - v_\infty + u_\infty(r_{S_\theta}/r_S)](r_{S_\theta}/r_S)}{[1 + (r_{S_\theta}/r_S)^2]} \tag{15}$$

Similarly,

$$v_2 = v_\infty + \left(1 - \frac{\rho_1}{\rho_2}\right) \times \frac{[r_{S_t} - v_\infty + u_\infty(r_{S_\theta}/r_S)]}{[1 + (r_{S_\theta}/r_S)^2]} \tag{16}$$

Pressure behind the shock is obtained from the MacCormack scheme at the predictor level. Once the pressure is known behind the shock, the normal component of the flow velocity ahead of the shock (measured with respect to the shock) can

be related to the pressure behind the shock by manipulating the oblique shock relations, which are

$$\rho_1 v_1 = \rho_2 v_2 \tag{17a}$$

$$p_1 + \rho_1 v_1^2 = p_2 + \rho_2 v_2^2 \tag{17b}$$

$$u_1 = u_2 \tag{17c}$$

$$h_1 + (V_1^2/2) = h_2 + (V_2^2/2) \tag{17d}$$

where V_1 and V_2 are resultant velocities. Utilizing these equations, one obtains

$$v_1 = \sqrt{\left(\frac{\gamma + 1}{2}\right) \frac{p_1}{\rho_1} \left(\frac{p_2}{p_1} + \frac{\gamma - 1}{\gamma + 1}\right)} \tag{18}$$

$$\frac{\rho_2}{\rho_1} = \frac{\dfrac{\gamma + 1}{\gamma - 1} \dfrac{p_2}{p_1} + 1}{\dfrac{\gamma + 1}{\gamma - 1} + \dfrac{p_2}{p_1}} = \frac{\dfrac{p_2}{p_1} + \dfrac{\gamma - 1}{\gamma + 1}}{1 + \dfrac{\gamma - 1}{\gamma + 1} \dfrac{p_2}{p_1}} \tag{19}$$

Equations (7), (15), (16), (18), and (19), when expressed in the notations of the advanced time level (in terms of the preceding time level), can be written as

$$r_S^{\overline{n+1}} = r_S^n + \Delta t r_{S_t}^n \tag{20}$$

$$V_{nnx,j}^{\overline{n+1}} = \sqrt{\left(\frac{\gamma + 1}{2}\right) \frac{p_\infty}{\rho_\infty} \left(\frac{p_{nnx,j}^{\overline{n+1}}}{p_\infty} + \frac{\gamma - 1}{\gamma + 1}\right)} \tag{21}$$

$$\frac{\rho_{nnx,j}^{\overline{n+1}}}{\rho_\infty} = \frac{\dfrac{p_{nnx,j}^{\overline{n+1}}}{p_\infty} + \dfrac{\gamma - 1}{\gamma + 1}}{1 + \dfrac{\gamma - 1}{\gamma + 1} \dfrac{p_{nnx,j}^{\overline{n+1}}}{p_\infty}} \tag{22}$$

$$u_{nnx,j}^{\overline{n+1}} = u_\infty - \left(1 - \frac{\rho_\infty}{\rho_{nnx,j}^{\overline{n+1}}}\right) \frac{\left[r_{S_{(j)}}^{\overline{n+1}} - v_\infty + u_\infty \left(\dfrac{r_{S_{\theta(j)}}^{\overline{n+1}}}{r_{S_{(j)}}^{\overline{n+1}}}\right)\right] \left(\dfrac{r_{S_{\theta(j)}}^{\overline{n+1}}}{r_{S_{(j)}}^{\overline{n+1}}}\right)}{\left[1 + \dfrac{r_{S_{\theta(j)}}^{\overline{n+1}}}{r_{S_{(j)}}^{\overline{n+1}}}\right]} \tag{23}$$

$$v_{nnx,j}^{\overline{n+1}} = v_\infty + \left(1 - \frac{\rho_\infty}{\rho_{nnx,j}^{\overline{n+1}}}\right) \frac{\left[r_{S_{(j)}}^{\overline{n+1}} - v_\infty + u_\infty \left(\dfrac{r_{S_{\theta(j)}}^{\overline{n+1}}}{r_{S_{(j)}}^{\overline{n+1}}}\right)\right]}{\left[1 + \left(\dfrac{r_{S_{\theta(j)}}^{\overline{n+1}}}{r_{S_{(j)}}^{\overline{n+1}}}\right)^2\right]} \tag{24}$$

It should be noted that i is normal to the body and varies from $i = 1$ at the surface to $i = nnx$ at the shock. Also, j is along the body and varies from $j = 1$ at the stagnation line to $j = nny$ at the outflow boundary.

Solution Procedure

Solution procedures are followed in four steps as described next.

Step 1: Initial Solution

The initial conditions for this calculation are obtained by using an approximate curve fit for the location and shape of the bow shock. Newtonian pressure distribution is used at the body. The approximate curve fit of Billig[24] is used to find r_S and r_{S_θ} along the shock. To find the initial conditions immediately behind the shock, r_{S_t} is set equal to zero and Eqs. (4)

and (21–24) are used. The initial flow conditions on the wall are obtained using the known wall temperature in conjunction with the pressure from the Newtonian pressure distribution. The initial flow conditions at interior grid points are obtained by assuming a linear variation between the flow conditions immediately behind the bow shock and the wall conditions.

Step 2: Predictor Step

At the beginning of the predictor step, the shock wave radial distance is computed from Eq. (9). The pressure immediately behind the shock $(p_{nnx,j}^{n+1})$ is computed using the MacCormack scheme[25]:

$$U_{nnx,j}^{\overline{n+1}} = U_{nnx,j}^{n} - (\Delta t/\Delta y)(F_{nnx,j+1}^{n} - F_{nnx,j}^{n})$$
$$- (\Delta t/\Delta x)(G_{nnx,j}^{n} - G_{nnx-1,j}^{n}) - \Delta t H_{nnx,j}^{n} \qquad (25)$$

Once the pressure behind the bow shock is obtained, $V_{nnx,j}^{\overline{n+1}}$ and $\rho_{nnx,j}^{\overline{n+1}}$ can be computed from the normal shock relations given by Eqs. (21) and (22). Similarly, the components of the fluid velocity behind the bow shock can be found from the oblique shock relations given by Eqs. (23) and (24). The remaining unknown $T_{nnx,j}^{\overline{n+1}}$ is calculated using the equation of state. This completes the predictor step.

Step 3: Corrector Step

The corrector step is similar to the predictor step except that the shock wave radial distance is evaluated using the modified Euler corrector, which is

$$r_{S_{(j)}}^{n+1} = r_{S_{(j)}}^{n} + (\Delta t/2)[r_{S_{k_{(j)}}}^{n} + r_{S_{k_{(j)}}}^{\overline{n+1}}] \qquad (26)$$

and Eq. (25) is replaced by the MacCormack corrector scheme in which the usual backward difference for $\partial G/\partial y$ is replaced by a forward difference given by

$$U_{nnx,j}^{n+1} = \tfrac{1}{2}[U_{nnx,j}^{n} + U_{nnx,j}^{\overline{n+1}} - (\Delta t/\Delta y)(F_{nnx,j}^{\overline{n+1}} - F_{nnx,j-1}^{\overline{n+1}})]$$
$$- \tfrac{1}{2}[(\Delta t/\Delta x)(G_{nnx,j}^{\overline{n+1}} - G_{nnx-1,j}^{\overline{n+1}}) + \Delta t H_{nnx,j}^{\overline{n+1}}] \qquad (27)$$

This completes the corrector step.

Step 4: Boundary Conditions

Once the calculation of boundary condition at $i = nnx$ (i.e., after the shock) has been performed by the shock-fitting method, the predictor or corrector steps are initiated at the interior grid points. All other boundary conditions are calculated after the predictor or corrector step is completed at all interior grid points.

The flow conditions along the supersonic outflow boundary (i.e., at $j = nny$) are determined by using a second-order extrapolation of interior grid point data.

Along the body surface the boundary conditions of no-slip, zero-pressure gradient, adiabatic, and noncatalytic wall were used.

Results and Discussion

Numerical computations were conducted to simulate Lehr's[4,5] experimental results. The physical and freestream conditions used in the simulations were $M_\infty = 5.11$ and 6.46, $P_\infty = 42,732$ N/m^2, $T_\infty = 292$ K, and $r_n = 15$ mm.

For the Mach 5.11 case, calculations were carried out on a grid of 101×101. Because of close coupling of bow-shock and reaction front (i.e., small induction distance) at high Mach numbers, a finer grid was needed to resolve the flowfield. Therefore, for Mach 6.46, a grid of 201×151 was used with 201 points in the circumferential direction and 151 points in the normal directions. The grids selected for the two cases were based on an earlier work by Ahuja et al.,[13] where a detailed grid refinement study (along with Fourier analysis for each grid) was done. This earlier work, which was based on
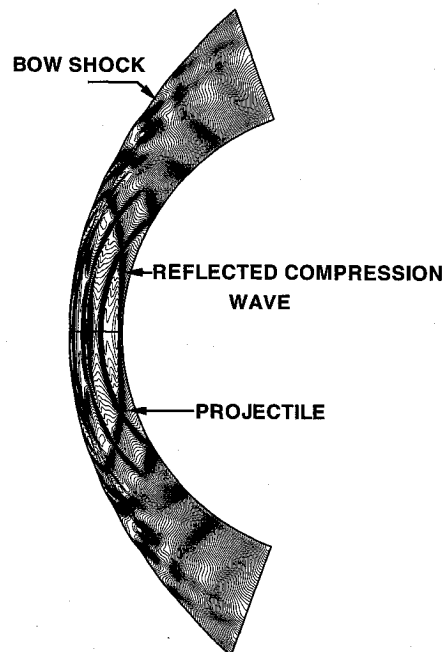

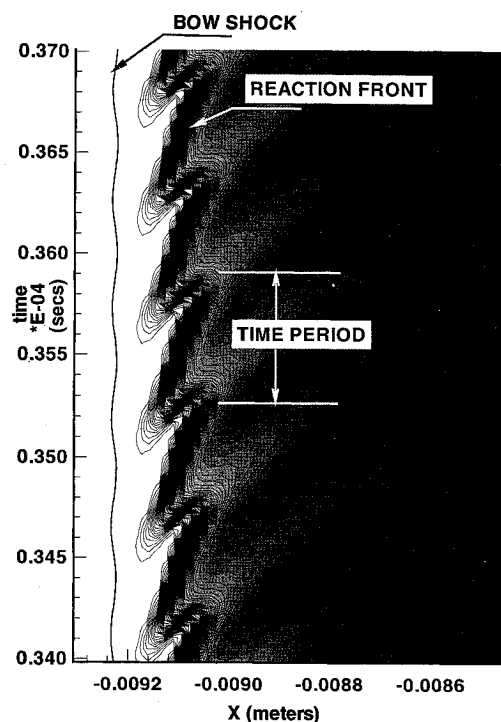Fig. 4 Enlarged pressure contours for Mach 5.11 case.

Fig. 5 Time history plot of water mass fraction for Mach 5.11.

shock-capturing method, used three different grids starting with a coarse grid of 101×78, which was refined to 131×101 and finally to 197×152. For the 101×78 grid, the Fourier analysis of the flowfield showed a fundamental frequency of 1.2 MHz. The calculations were repeated for a finer grid of 131×101, while maintaining the same grid aspect ratio as in the previous case, and showed a fundamental frequency of 2 MHz. The previous calculations were repeated on yet another refined grid of 197×152 and the fundamental frequency on this grid was 2.1 MHz. Thus, refining the grid from 131×101 to 197×152 did not change the frequency appreciably and, therefore, the solution was considered grid independent and physical on the finest grid. In shock fitting, since there are no grid points beyond the bow shock, a grid
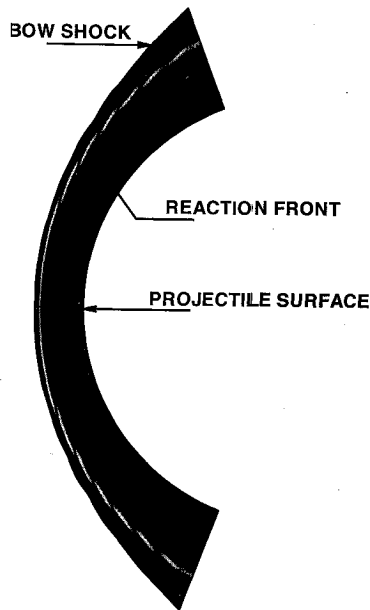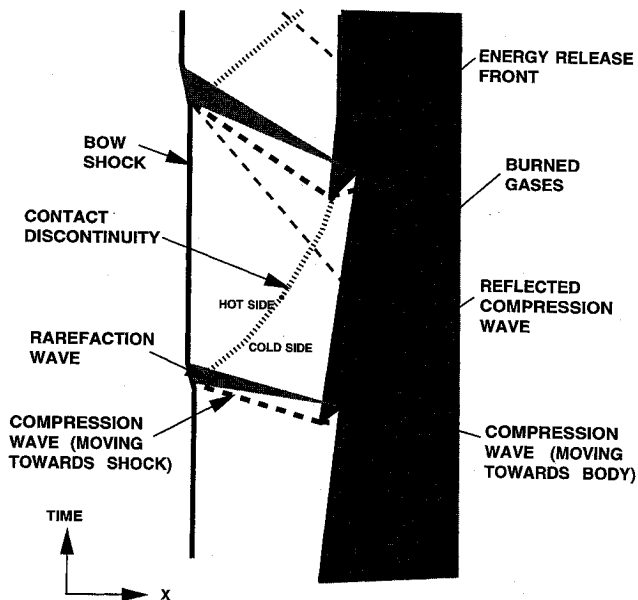
Fig. 6 Computed shadowgraph for Mach 5.11.

Fig. 7 One-dimensional wave interaction model.

of 101 × 101 for Mach 5.11 and 201 × 151 for Mach 6.46 was found sufficient to adequately resolve the flowfield.

Figure 4 shows the pressure contour plots for the Mach 5.11 case. The complicated wave pattern seen can be viewed as made up of two types of compression waves. One type of compression wave originates from the reaction front, whereas the other has been reflected from the projectile body. The reflected compression wave interacts with the original compression wave and, at the point of interaction, two new waves are generated. This reflection produces the observed cell structure. The compression wave that moves towards the bow shock, overtakes it, and causes the bow shock to move forward. Thus, the kinks appearing on the bow shock are due to some of its structure being distorted by the compression waves. Figure 4 also reveals that these pulsations in the reaction front are strong near the nose region and dissipate near the shoulder regions of the projectile.

To help understand the temporal nature of these instabilities, attention is now focused on the time history of physical variables along the stagnation line. Figure 5 shows the time history

plot of water mass-fraction along the stagnation streamline. Two discontinuities are seen clearly. The outer discontinuity is the bow shock, which shows little kinks in the structure, and the inner discontinuity is the reaction front. The highly periodic oscillations in the reaction front that originate near the stagnation line and then spread downstream are clearly evident. It is noted that the frequency of oscillation can be calculated directly from the plot. This frequency is 2.0 MHz, whereas the experimental frequency from Lehr's ballistic data for Mach 5.11 case is 1.96 MHz. Also, the amplitude of the oscillations of reaction front is about 8.0×10^{-5} m. According to McVey and Toong's wave interaction model, the period of
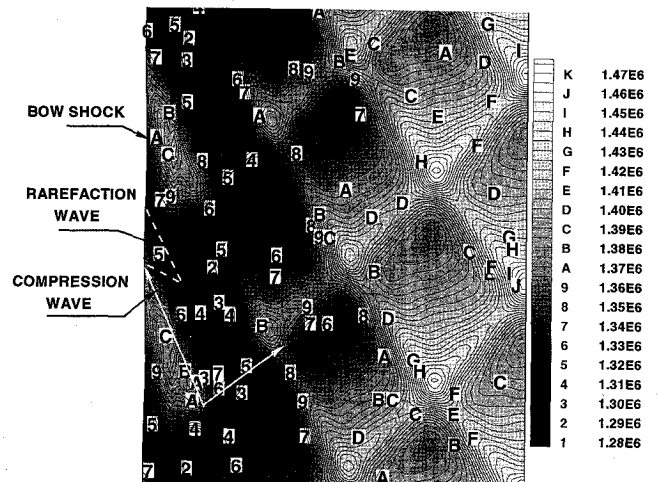

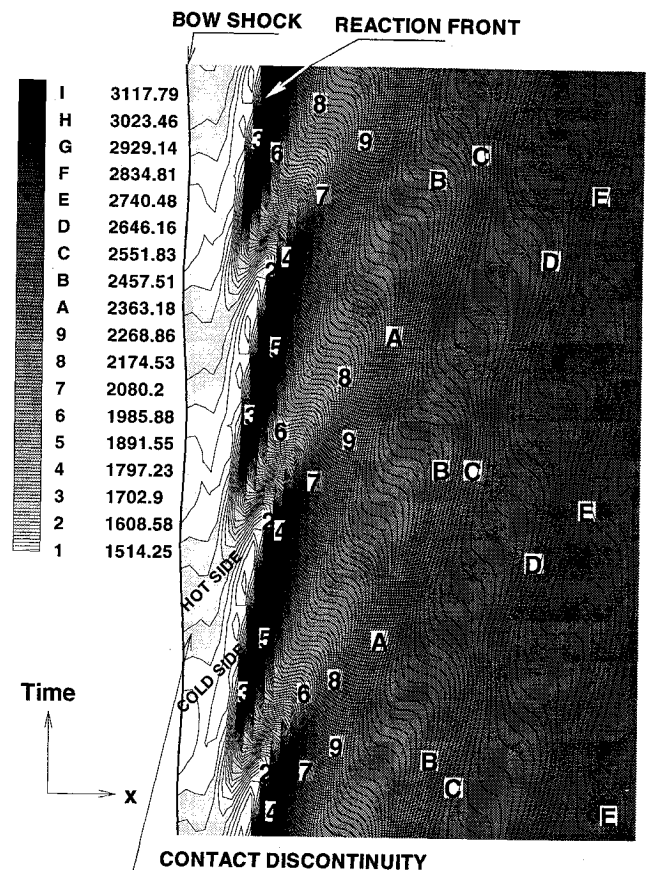Fig. 8 Time history plot of pressure along the stagnation line for Mach 5.11.

Fig. 9 Time history plot of temperature along the stagnation line for Mach 5.11.

oscillation is approximately 1.67 times the induction time corresponding to the postshock conditions, i.e.,

$$\tau/\tau_s = 1.67$$

where τ is the period of wave interaction and τ_s is the induction time behind the normal portion of the bow shock.

For Mach 5.11, the postshock Mach number is approximately 0.4 and the length of the induction zone Δl is estimated to be

$$\Delta l = u_s\tau_s = 0.4a_s\tau_s$$

where u_s is the fluid velocity behind the bow shock and a_s is the speed of sound in the induction zone. From Fig. 5, it is clear that $\Delta l \approx 1.5 \times 10^{-4}$ m and postshock temperature T_s is 3150 K; therefore, the speed of sound $a_s = \sqrt{\gamma RT_s} = \sqrt{1.36 \times 397.474 \times 3150} = 1304.9$ m/s. This gives $\tau_s = 2.87 \times 10^{-7}$ s, and hence, $\tau = 1.67\tau_s = 4.8 \times 10^{-7}$ s. Therefore, oscillation frequency for Mach 5.11 from McVey and Toong's model is about 2.08 MHz, which is in good agreement with the calculated frequency of 2.0 MHz and the experimental frequency of 1.96 MHz.

The computed shadowgraph for the Mach 5.11 case is shown in Fig. 6. The presence of two discontinuities is clearly evident. The outer discontinuity is the bow shock and the inner discontinuity is the reaction front. It is seen that the bow shock and the reaction front are separated from each other near the stagnation line, and this separation keeps increasing downstream of the stagnation line. This is exactly what was observed experimentally in Lehr's work. Also, the bow shock is quite smooth with very little waviness, but the reaction front clearly shows a periodic behavior. The instability is characterized by an almost regular periodic wave motion having a constant frequency, similar to that observed experimentally.

By means of time history plots, a comparison of the numerical results with the wave-interaction model originally proposed by McVey and Toong,[6] and further modified by Matsuo and Fujiwara,[11] can be made. The essential features of this one-dimensional model are shown in Fig. 7. To understand how the wave interaction model fits with the numerical results, it is also essential to consider the results presented in Figs. 8 and 9.

Figure 8 shows the time history plot for the pressure along the stagnation streamline (showing the actual numerical values of pressure). The time history plots of temperature, along the stagnation streamline, are presented in Fig. 9. By comparing the actual model shown in Fig. 7 with the $x-t$ diagrams of pressure and temperature shown in Figs. 8 and 9, it can be demonstrated that the model proposed by McVey and Toong fits very well with the present numerical calculations.

As shown in Fig. 7, a contact discontinuity first approaches the original reaction front. The gases are hot on the upstream side of the contact discontinuity and comparatively cold on the lower side (see also Fig. 9). These hot gases behind the contact discontinuity begin to react, generating compression or pressure waves that propagate both upstream and downstream, as seen in Fig. 8. The compression wave that propagates upstream intersects with the bow shock and produces a contact discontinuity behind the bow shock. The bow shock is stronger after the interaction and, therefore, the gas is hotter on the upstream side of the contact discontinuity. The hot gases behind the contact discontinuity reduce the induction time and create a new reaction front, generating another set of compression waves. At a later time, the contact discontinuity reaches the position of the original reaction front, extinguishing the reaction at this point because no more unreacted mixture exists there. The rate of energy release is effectively reduced, which generates rarefaction waves (Fig. 8). The reaction front begins to recede because of increasing induction time of the colder fluid. The compression wave traveling towards the blunt body gets reflected from the body, travels back to the bow shock, and interacts with it at about the same time that the most recently created compression wave arrives at the bow shock. The compression wave and the reflected compression wave from the body interact with the bow shock, providing a possible mechanism for the creation of another contact discontinuity, i.e., secondary contact discontinuity. The gases, being hotter on the upstream side of the contact discontinuity, start burning again, generating compression waves; the cycle is then repeated as shown in Figs. 8 and 9. Matsuo and Fujiwara[11] also emphasized the importance of considering the reflection of the compression wave from the body in their calculations. The compression wave reflected from the blunt body may not necessarily be in phase with the compression waves created by the new energy release front. Thus, once these reflected waves interact, they cause the flow to be not exactly periodic; however, the pulsating energy release front could still be nearly periodic.
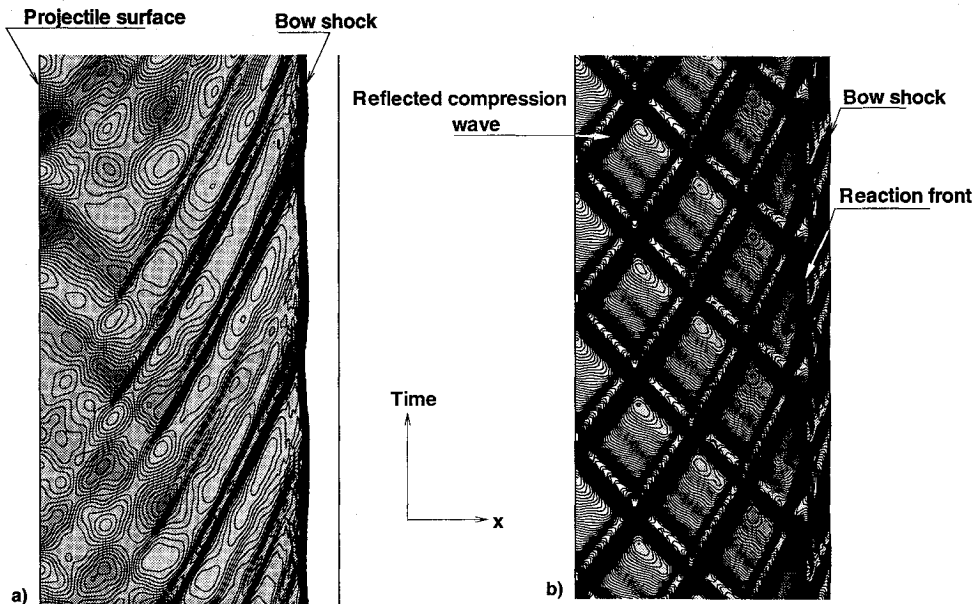

Fig. 10   Time history plots for pressure for Mach 5.11 with a) shock-capturing (grid 197 × 152) and b) shock-fitting method (grid 101 × 101).
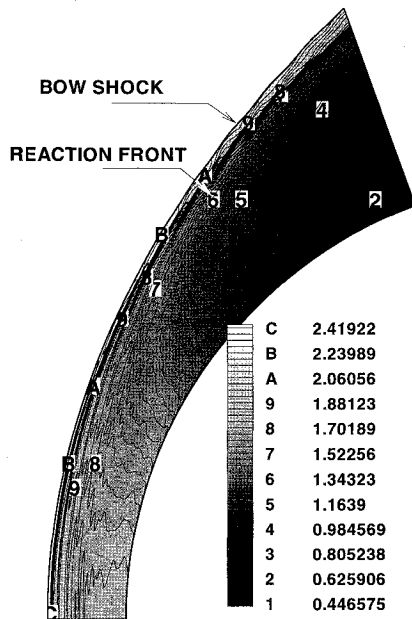
Fig. 11 Density contours for Mach 6.46.

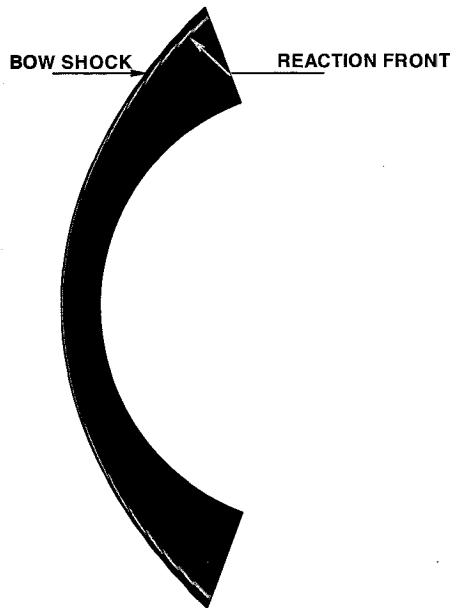Fig. 12 Computed shadowgraph for Mach 6.46.

Fig. 13 Time history plot of water mass fraction along stagnation line for Mach 6.46.

A comparison of results obtained by the shock-fitting and shock-capturing techniques can be done by referring to Fig. 10. Figure 10a shows the time history plot for pressure for Mach 5.11 along the stagnation line obtained by using the shock-capturing technique and a grid of 197 × 152, while Fig. 10b shows the same results as obtained by using the shock-fitting technique and a grid of 101 × 101. Comparing these results it is seen that all of the flow features between the bow shock and the reaction front are clearly depicted in Fig. 10b, whereas most of the flow features are smeared in Fig. 10a. It should be noted also that the number of grid points used in the shock-fitting technique is almost one-third of that used in the shock-capturing technique and still the resolution with shock fitting is much better than with shock capturing.

The results for the Mach 6.46 case are now presented. This is a superdetonative case, i.e., the projectile velocity is higher than the C–J velocity of the mixture. The density contours are shown in Fig. 11. The bow shock and the reaction front are seen to be almost coupled with each other. For this case, a very small induction distance occurs as a result of the post-
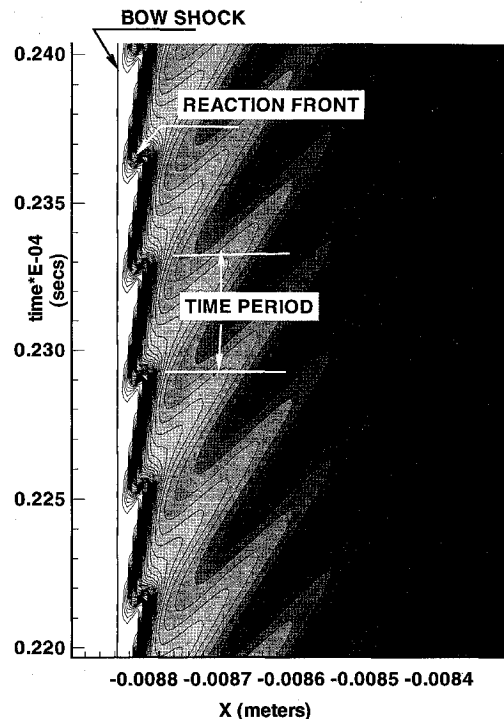
shock temperature remaining significantly high up to some distance downstream of the stagnation zone. Away from the stagnation line, the induction distance is increased as a result of the decreasing shock strength and postshock temperature. The bow shock has a very crisp and smooth profile. The reaction front, which is smooth up to about 60–65 deg from the nose region, is wrinkled with very small amplitude waves downstream.

Figure 12 shows the computed shadowgraph for the Mach 6.46 case. Although observed experimentally that the bow shock and the reaction fronts are smooth, numerical results show slight unsteadiness in the reaction front, and this could be attributed to very high-frequency and very low-amplitude oscillations. The current computed shadowgraph is amplified many times more than the experimental shadowgraph. Consequently, the high-frequency oscillations observed numerically are evident in the computed shadowgraph. Thus, the Mach 6.46 case can be considered as a macroscopically stable case, i.e., the one with very high-frequency and low-amplitude reaction front unsteadiness.

Figure 13 shows the time history plot for water mass fraction. The bow shock is 0.00884 m from the center of the blunt body. The distance between the bow shock and the reaction front is very small. Also, as seen from the figure, the amplitude of oscillations of the reaction front is 2.5 × 10⁻⁵ m. This is quite small compared with the Mach 5.11 case. The frequency of oscillations can be computed directly from the figure and is found to be 2.85 MHz, which is comparable with the earlier work.[14] Thus, the Mach 6.46 case is a very high-frequency but very low-amplitude phenomena. Experimental fundamental frequency for the Mach 6.46 case is not available.

Conclusions

A shock-fitting technique has been used to simulate the shock-induced combustion past blunt projectiles. In such problems that involve instabilities, the shock-fitting technique gives much better resolution of the flow features than the shock-capturing technique. The observed flow features have been successfully correlated with the one-dimensional wave-interaction model, and the frequency of oscillations has been

matched with the experimental data as well as with earlier investigations.

References

[1]Cambier, J. L., and Adelman, H., ''Numerical Simulations of an Oblique Detonation Wave Engine,'' AIAA Paper 88-0063, Jan. 1988.

[2]White, M. E., Drummond, J. P., and Kumar, A., ''Evolution and Status of CFD Techniques for Scramjet Applications,'' AIAA Paper 86-0160, Jan. 1986.

[3]Atamanchuk, T., and Sislian, J., ''On-and-Off Design Performance Analysis of Hypersonic Detonation Wave Ramjets,'' AIAA Paper 90-2473, July 1990.

[4]Lehr, H. F., ''Experiments on Shock-Induced Combustion,'' *Acta Astronautica*, Vol. 17, Sept. 1972, pp. 589–597.

[5]Anon., ''Rapport-Bericht CO 7/73,'' Inst. Saint Louis, Final Rep. 20/71, Saint Louis, France, July 1971; also Dissertation, Karlsruhe, Germany, 1971.

[6]McVey, J. B., and Toong, T. Y., ''Mechanism of Instabilities of Exothermic Hypersonic Blunt-Body Flows,'' *Combustion Science and Technology*, Vol. 3, No. 2, 1971, pp. 63–76.

[7]Alpert, L. R., and Toong, T. Y., ''Periodicity in Exothermic Hypersonic Flows About Blunt Projectiles,'' *Acta Astronautica*, Vol. 17, Sept. 1972, pp. 539–560.

[8]Wilson, G. J., and MacCormack, R. W., ''Modelling Supersonic Combustion Using a Fully-Implicit Numerical Method,'' *AIAA Journal*, Vol. 30, No. 4, 1992, pp. 1008–1015.

[9]Sussman, M. A., ''Source Term Evaluation for Combustion Modelling,'' AIAA Paper 93-0239, Jan. 1993.

[10]Wilson, G. J., and Sussman, M. A., ''Computation of Unsteady Shock-Induced Combustion Using Logarithmic Species Conservation Equations,'' *AIAA Journal*, Vol. 31, No. 2, 1993, pp. 294–301.

[11]Matsuo, A., and Fujiwara, T., ''Numerical Simulations of Shock-Induced Combustion Around an Axisymmetric Blunt Body,'' AIAA Paper 91-1414, June 1991.

[12]Matsuo, A., and Fujiwara, T., ''Numerical Investigation of Oscillatory Instability in Shock-Induced Combustion Around a Blunt Body,'' *AIAA Journal*, Vol. 31, No. 10, 1993, pp. 1835–1841.

[13]Ahuja, J. K., and Tiwari, S. N., ''Investigation of Hypersonic Shock-Induced Combustion in a Hydrogen-Air System,'' AIAA Paper 92-0339, Jan. 1992.

[14]Ahuja, J. K., and Tiwari, S. N., ''Numerical Simulation of Shock-Induced Combustion in a Superdetonative Hydrogen-Air System,'' AIAA Paper 93-0242, Jan. 1993.

[15]Singh, D. J., Ahuja, J. K., and Carpenter, M. H., ''Numerical Simulations of Shock-Induced Combustion/Detonation,'' *Computing Systems in Engineering*, Vol. 3, Nos. 1–4, 1992, pp. 201–215.

[16]Matsuo, A., Fujiwara, T., and Fujii, K., ''Flow Features of Shock-Induced Combustion around Projectiles Travelling at Hypervelocities,'' AIAA Paper 93-0451, Jan. 1993.

[17]Ahuja, J. K., and Tiwari, S. N., ''A Parametric Study of Shock-Induced Combustion in a Hydrogen-Air System,'' AIAA Paper 94-0674, Jan. 1994.

[18]Kumar, A., and Singh, D. J., ''Unsteady Shock-Induced Combustion Past Blunt Bodies,'' *Proceedings of the ICASE/LaRC Workshop on Transition, Turbulence, and Combustion*, Vol. II, Kluwer Academic, Norwell, MA, 1994, pp. 289–300.

[19]Tivanov, G., and Rom, J., ''Analysis of the Stability Characteristics of Hypersonic Flow of a Detonable Gas Mixture in the Stagnation Region of a Blunt Body,'' AIAA Paper 93-1918, June 1993.

[20]Matsuo, A., Fujii, K., and Fujiwara, T., ''Computational Study of Unsteady Combustion Around Projectiles with Emphasis on the Large-Disturbance Oscillation,'' AIAA Paper 94-0764, Jan. 1994.

[21]Ruegg, F. W., and Dorsey, W., ''A Missile Technique for the Study of Detonation Waves,'' *Journal of Research of the National Bureau of Standards*, Vol. 66C, No. 1, 1962, pp. 51–58.

[22]Drummond, J. P., Rogers, R. C., and Hussaini, M. Y., ''A Detailed Numerical Model of a Supersonic Reacting Mixing Layer,'' AIAA Paper 86-1427, June 1986.

[23]Jachimowski, C. J., ''An Analytical Study of the Hydrogen-Air Reaction Mechanism with Application to Scramjet Combustion,'' NASA TP-2791, Feb. 1988.

[24]Billig, S. F., ''Shock-Wave Shapes Around Spherical and Cylindrical-Nosed Bodies,'' *Journal of Spacecraft*, Vol. 4, No. 6, 1967, pp. 822, 823.

[25]MacCormack, R. W., ''The Effect of Viscosity in Hypervelocity Impact Cratering,'' AIAA Paper 69-354, April 1969.